Research Square

Preprints are preliminary reports that have not undergone peer review.
They should not be considered conclusive, used to inform clinical practice,
or referenced by the media as validated information.

Transcranial optical and optoacoustic super-resolution cortical microangiography in aged and Alzheimer mice

Lin Tang
University of Zurich
Quanyu Zhou
University of Zurich
Daewoon Seong
University of Zurich
Leon Nhan
University of Zurich
Daniel Razansky
University of Zurich
Xose Luis Dean-Ben
xl.deanben@pharma.uzh.ch
University of Zurich

Article

Keywords: Diffuse optical localization imaging (DOLI), localization optoacoustic tomography (LOT), cortical microvasculature, blood flow velocity, aging, Alzheimer's disease (AD).

Posted Date: November 4th, 2026

DOI: https://doi.org/10.21203/rs.3.rs-11333091/v1

License: This work is licensed under a Creative Commons Attribution 4.0 International License.
Read Full License

Additional Declarations: No competing interests reported.

Abstract

Cerebrovascular alterations and dysfunction are increasingly recognized as key contributors to aging and Alzheimer's disease (AD), yet longitudinal *in vivo* imaging of cortical microvascular networks remains challenged by limited penetration of ballistic photons and transcranial ultrasound aberrations. While super-resolution ultrasound (SRUS) has enabled unprecedented capabilities for microangiography via microbubble localization and tracking, aberrations arising from bidirectional ultrasound propagation through the thickened skull of aged mice remain a significant challenge, often necessitating cranial windows. Here, we propose a complementary localization-based framework combining diffuse optical localization imaging (DOLI) and localization optoacoustic tomography (LOT) for super-resolution vascular imaging in aged and AD mice. DOLI capitalizes on the reduced light scattering in the second near-infrared window (NIR-II) to achieve transcranial visualization of the cortical microvasculature, while LOT leverages the unidirectional ultrasound propagation in optoacoustics to resolve pial microvessels and penetrating branches in a fully non-invasive manner. Both modalities reveal structural microvascular alterations in aging and AD, including increased vessel convolution and tortuosity at different scales, highlighting their potential for longitudinal studies of cerebrovascular pathology.

Introduction

Increasing evidence highlights the critical role of cerebrovascular alterations in the aging brain and in neurodegenerative disorders such as Alzheimer's disease (AD) [1–3]. Cerebral vascular alterations are hypothesized to actively promote neuronal dysfunction and degeneration, rather than simply reflect downstream consequences [4,5]. Clinical and preclinical studies support this view, showing that reduced cerebral blood flow and impaired cerebrovascular reactivity are associated with worsened cognitive performance in both normal aging and pathological states [6–8]. Moreover, microvascular abnormalities, including altered capillary morphology, reduced perfusion, and disrupted hemodynamics, have been linked to accelerated disease progression and cognitive impairment [9–11].

Aging itself is accompanied by profound changes in cerebrovascular structure and function [12]. These include vessel rarefaction, increased tortuosity, and diminished vascular elasticity, all of which can compromise cerebral perfusion [13]. Such alterations are thought to play a central role in the development of vascular cognitive impairment and dementia, a condition of increasing prevalence in aging populations [14]. In the context of AD, accumulating evidence indicates that cerebrovascular dysfunction is tightly coupled to disease progression [15,16]. Both patients and animal models exhibit reduced vascular density, abnormal vessel morphology, and impaired microcirculatory flow, suggesting that vascular pathology is an integral component of the disease process [17,18]. Importantly, these changes may precede neuronal loss, underscoring the need for imaging techniques capable of resolving microvascular architecture and dynamics *in vivo*.

Despite its importance, the study of microvascular changes in the brain has been limited by technical challenges. Optical imaging modalities are inherently limited in penetration depth, restricting their ability to non-invasively access the murine brain. Even techniques such as optical coherence tomography angiography (OCTA) and two-photon microscopy (2PM), which can reach relatively greater depths than other optical approaches, remain constrained in brain microangiography applications due to their reliance on cranial windows, thereby hampering longitudinal investigations [19–21]. Visualization of the cerebral microvasculature requires thus methods that can penetrate deep tissue while maintaining sufficient spatial resolution. Super-resolution ultrasound (SRUS) has emerged as a powerful modality in this context, enabling visualization of microvascular networks and flow dynamics at unprecedented resolution *in vivo* [22,23]. SRUS has provided valuable insights into subcortical vascular organization and function [24], offering a means to characterize vascular phenotypes associated with aging and neurodegeneration [25–30]. However, the application of SRUS in longitudinal and translational studies faces significant limitations. In particular, imaging through the intact skull remains challenging, especially in aged animals where skull thickening leads to increased acoustic attenuation and aberration. As a result, invasive procedures such as acoustic cranial window implantation or skull thinning have been required, which can introduce distortions in physiological parameters and limit applicability in studies of aging and disease progression.

To address these challenges, there is a need for imaging approaches capable of resolving cortical microvasculature with high fidelity in a non-invasive manner. Recently, localization-based imaging techniques analogous to SRUS have been introduced for super-resolution microangiography. In particular, diffuse optical localization imaging (DOLI) and localization optoacoustic tomography (LOT) have been shown to be capable of visualizing the cortical microvasculature through the intact scalp and skull [31–34]. In this work, we employ DOLI and LOT as complementary modalities to image the mouse brain cortex in aged and AD mice without skull thinning or cranial window implantation. This enables *in vivo* characterization of vascular structure, density, and flow velocity, providing new opportunities to investigate microvascular alterations associated with aging and AD.

Results

Large-scale transcranial visualization of microvascular alterations with diffuse optical localization imaging

DOLI exploits the reduced scattering and autofluorescence in a so-called second near-infrared (NIR-II, 900–1700 nm) window to achieve greater depths than other fluorescence imaging approaches operating at shorter wavelengths, enabling e.g. visualization of the murine cortical microvasculature through the intact scalp and skull [31]. DOLI is implemented in an epi-illumination configuration, where a short-wave infrared (SWIR) camera collects the long-pass filtered fluorescence responses from the tissue being excited with a continuous-wave (CW) laser at 795 nm (Fig. 1a, see methods for details). In the experiments conducted in this study using AD and wild-type (WT) aged mice, the scalp was removed to

improve imaging contrast. For each mouse, a sequence of images was acquired following the injection of dichloromethane droplets containing quantum dots with a peak fluorescence emission at 1600 nm. The acquired sequence of images was first filtered to remove background signals and subsequently processed to localize and track microdroplets flowing in the bloodstream (Fig. 1b, see methods for details). The DOLI image is formed by accumulating the positions of localized droplets, while tracking further enables the generation of blood velocity maps and the assessment of flow direction. Convoluted and tortuous vessels were consistently observed in AD and aged WT mice in the DOLI images of the cortical microvasculature (Fig. 1c and Suppl. Figure 1), implying structural remodeling of the brain vasculature. Although not uniformly distributed across the brain, such morphological alterations are expected in association with aging and amyloid/tau pathology. Zoomed-in views of selected regions further confirm the presence of convoluted and tortuous vessels within finer microvascular networks (Fig. 1d). Non-invasive transcranial visualization of such small-scale alterations is generally not feasible with other microscopic imaging modalities due to optical and acoustic aberrations introduced by the thick skull of aged mice. Tortuosity is linked to altered hemodynamics, including reduced effective perfusion and abnormal flow velocity distributions, which can exacerbate tissue hypoxia and promote pathology. A slightly reduced average blood flow velocity was observed in AD mice relative to age-matched WT mice in approximately matched brain regions (Fig. 1e, mean ± std values 10.4 ± 1.58 mm/s vs 9.5 ± 1.32 mm/s for WT and AD mice, respectively), consistent with observations obtained using ultrasound flow imaging [27]. Cerebrovascular remodeling also implies reduced vessel diameter, altered branching patterns, and changes in vessel density. The vessel density (vascularity) in the selected regions was estimated as the number of pixels containing vessels, normalized to the average value in WT mice. No significant differences were observed between WT and AD mice (Fig. 1e, mean ± std values 1 ± 0.12 vs 0.96 ± 0.17 for WT and AD mice, respectively). On the other hand, vessel tortuosity was estimated as the sum of angular changes along vessels within the selected regions, normalized to the average value in WT mice (see methods for details). Also, no significant differences were observed between WT and AD mice (Fig. 1e, mean ± std values 1 ± 0.43 vs 0.99 ± 0.18 for WT and AD mice, respectively).

Non-invasive whole-cortex coverage with localization optoacoustic tomography

Similar to DOLI or SRUS, LOT relies on localization and tracking of individual microparticles that are sufficiently small to traverse microvascular networks, while generating sufficiently strong signals to enable reliable detection at the single-particle level. Multiple types of particles with strong absorption in the NIR-II spectral range have recently been developed to meet these requirements. Among these, the calcium carbonate microparticles loading copper sulfide nanoparticles employed in this study offer a suitable combination of optical contrast and biocompatibility for reliable single-particle detection at 1064 nm, corresponding to the fundamental wavelength emitted by standard short-pulsed Nd:YAG lasers lying in a spectral range where water absorption is reduced [35]. LOT is implemented with an optoacoustic (OA) tomographic imaging system based on a spherical array of piezocomposite elements (Fig. 2a, see

methods for details) [36]. The field of view (FOV) for particle detection is determined by the per-particle absorption, the sensitivity field of the array, and the intensity and spatial distribution of the incident laser beam. Typically, particles can be detected in the mouse brain within a volume of approximately 5 mm in diameter and 2–3 mm in depth below the skin for a single array position. A larger FOV can be achieved by mechanically scanning the array across multiple positions covering the mouse cortex (Fig. 2b). For each position of the array, different types of images can be rendered from the sequence of frames acquired following intravenous injection of a bolus of particles. The motion-contrast optoacoustic (MCOA) image is reconstructed from a compounded sequence of singular value decomposition (SVD)-filtered OA images (Fig. 2c). The combination of the MCOA images corresponding to different positions of the array enables visualizing of vascular networks across the entire murine cortex. Generally, MCOA images improve the vessel visibility relative to standard OA images affected by limited-view effects and lack of contrast from small vessels [34]. From the same filtered image sequences, LOT images are reconstructed by accumulating the positions of localized particles, and can be further combined across multiple positions to provide whole-cortex coverage of microvascular networks (Fig. 2d). LOT provides a more detailed view of smaller pial vessels, including venules, arteries, and penetrating branches across the cortical surface. Importantly, the unidirectional propagation of ultrasound waves in OA imaging reduces transcranial distortion compared with SRUS, enabling accurate microvascular imaging with LOT through the intact scalp and skull [37]. This fully non-invasive approach thus facilitates longitudinal imaging of disease progression. Much like in DOLI, velocity maps can also be calculated, which can also expand across the entire cortex via combination of several images (Fig. 2e). It is important to note that higher accuracy in velocity estimation is expected in three-dimensional imaging due to the arbitrary orientation of vascular networks in multiple directions.

Volumetric assessment of microvascular remodeling in superficial and penetrating vessels

The three-dimensional images provided by LOT allow for accurate and high-resolution visualization of the microvascular morphology of vascular networks, including complex architectures that expand and branch in arbitrary spatial directions. Specifically, penetrating arterioles and venules that traverse from the pial surface into the cortical parenchyma are a fundamental functional component of the cortical microcirculation that cannot be captured in the two-dimensional images provided by DOLI. For a detailed assessment of the murine cortical microvasculature, we focused on brain regions centered on the anterior-posterior axis and laterally shifted on the medial-lateral axis in both AD and WT mice (Fig. 3a and c). Much like for the images acquired with DOLI, the maximum intensity projection (MIP) along the depth direction of the LOT images of AD mice consistently show convoluted and tortuous vessels in the cortical surface associated to the expected structural reconfiguration of the cerebral vascular system (Fig. 3a and Suppl. Figure 2). The MIPs of the blood flow velocity maps from the same region provide an additional cross-check of the DOLI observations, demonstrating good agreement between the two modalities. Microvascular alterations in penetrating cortical vessels could also be assessed using LOT

images. Tortuosity in these microvessels is evident in selected cross-sectional views of the reconstructed microvascular maps, obtained as MIPs over a thickness of 400 μm along the horizontal and vertical directions (Fig. 3b). Deep cortical penetrating arterioles and capillary networks show greater vulnerability to AD-related pathological processes than superficial or larger vessels [34], making their tortuosity particularly informative for understanding disease mechanisms and for developing biomarkers and therapeutic readouts. Analogous alterations were observed in age-matched WT mice, with microvascular structures exhibiting increased convolution and tortuosity across spatial scales, evident in both superficial (Fig. 3c) and penetrating (Fig. 3d) vessels, in line with expected features of vascular aging [26]. Comparison of measured blood flow velocities, vascular density (vascularity), and vessel tortuosity in selected regions of AD and WT mice, approximately corresponding to those analyzed with DOLI, yielded results consistent with those obtained with the DOLI images (Fig. 3e). Specifically, slightly lower values in velocity (mean ± std values 9.59 ± 0.67 mm/s vs 9.26 ± 1.36 mm/s for WT and AD mice, respectively), vascularity (mean ± std values 1 ± 0.67 vs 0.76 ± 0.65 for WT and AD mice, respectively), and tortuosity (mean ± std values 1 ± 0.23 vs 0.95 ± 0.41 for WT and AD mice, respectively), were observed in AD relative to WT mice, although no significant differences were observed. Notably, a significant difference between the measured velocities in AD and WT mice was observed if the values measured with DOLI and LOT are combined (Suppl. Figure 3). Indeed, velocity measurements arguably represent the most robust parameter, as vascular density depends on the number of injected particles, which may vary between batches, and tortuosity can only be reliably assessed in a subset of vessels across the brain.

Discussion

Both LOT and DOLI have been shown to enable visualization of cortical microvasculature in aged mice with intact, thick skulls, including both healthy and AD models. Imaging and histological studies in AD consistently report cortical abnormalities, including altered capillary density, disrupted vascular architecture, and blood-brain barrier (BBB) dysfunction, highlighting the cortex as a primary site of disease-related vascular pathology [38–42]. The cortex contains a dense capillary network to efficiently support high synaptic activity. Aging-related capillary rarefaction, endothelial dysfunction, and pericyte loss disproportionately affect cortical gray matter, contributing to regional hypoperfusion, metabolic stress, and vulnerability to amyloid beta (Aβ) deposition and tau pathology in AD [43–45]. Recent studies highlight the preferential vulnerability of deep cortical layers to aging-associated alterations [46–48]. Cerebral angiopathy in AD was also shown to predominantly affect the cerebral leptomeninges and the cortex [5]. Recognition of the cortex as a key site of microvascular pathology provides a foundation for biomarker development, improved risk stratification, and the design of vascular-targeted therapies to attenuate age-related cognitive decline and AD progression.

LOT relies on highly absorbing particles that generate sufficiently strong OA signals to be individually detected against the background signals from blood. A variety of particle types have been employed for LOT [35,49–52], with the achievable imaging depth determined by the particle properties, as well as the

illumination conditions, including light intensity, beam profile at the tissue surface, and optical wavelength. Using the particles selected in this study, imaging depths of approximately 3 mm have been achieved in the highly absorbing murine brain. In aged mice, this depth may be limited by increased skull thickness (typically ~ 300 µm [53]), which can attenuate and distort ultrasound propagation. Notably, in contrast to SRUS, LOT relies on unidirectional ultrasound propagation, thereby reducing transcranial acoustic aberrations. Consistent with this, LOT has been shown to provide higher vascular contrast and resolution in the aged mouse cortex compared to SRUS when using the same spherical array [37]. The topical application of chemical agents may further increase the acoustic transparency of the skull and further reduce aberrations [54]. In its current implementation, LOT enables coverage of the entire murine cortex, facilitating the identification of vascular changes associated with aging and disease progression. Further increases in imaging depth may be achievable through the use of highly absorbing particles and longer excitation wavelengths (e.g., ~ 1064 nm), where optical attenuation is reduced.

DOLI similarly relies on microdroplets that are sufficiently small to traverse microvascular networks while generating signals strong enough for individual detection. In this case, the droplets emit fluorescence responses in the NIR-II spectral window (900–1700 nm), which offers a promising approach for deep-tissue optical imaging beyond the conventional penetration limits of fluorescence microscopy. The development of sensitive SWIR cameras operating in this range has enabled imaging in a regime characterized by reduced scattering and autofluorescence, thereby facilitating deeper penetration of ballistic photons. As in LOT, the achievable imaging depth in DOLI is governed by droplets properties, particularly fluorescence intensity and emission wavelength, as well as illumination conditions, including light intensity and beam profile. Ongoing efforts continue to expand the range of suitable contrast agents [55]. In this work, the scalp was removed to optimize imaging through the thick skull of aged mice. However, DOLI has been demonstrated to be applicable in a fully non-invasive manner [31]. Currently, DOLI enables imaging depths of approximately 2 mm in the murine brain, with potential for further improvement as new materials emitting in the NIR-II window are developed. In addition, three-dimensional imaging has been demonstrated using a stereovision-based approach with two cameras [32].

In summary, this work demonstrates the potential of LOT and DOLI as complementary, minimally invasive imaging modalities for resolving cortical microvascular architecture in aged and AD mouse models. By enabling high-resolution angiography through the intact skull, these approaches overcome key limitations of existing techniques and provide access to cortical vascular alterations *in vivo*. Together, they offer a powerful framework for advancing our understanding of cerebrovascular contributions to aging and neurodegeneration, with promising implications for longitudinal research and translational studies.

Methods

Diffuse optical localization imaging

DOLI was implemented using an epi-fluorescence (widefield) configuration [31]. Excitation was provided by a CW laser (CNI Lasers Co. Ltd., Changchun, China) operating at 795 nm, with the beam expanded to achieve an average power density of 300 mW/cm^2. The emitted fluorescence response was filtered using a long-pass filter (FEL1100, Thorlabs, USA) and imaged with an NIR-II–optimized lens (LM50HCSW, 50 mm focal length, Kowa, Japan) at a magnification of ~ 0.35–0.5. Images were acquired using an InGaAs-based SWIR camera (WiDy SenS 640V-ST, NiT, France) operated in linear mode with air cooling at − 15°C. The camera features a 15 µm pixel pitch and a native resolution of 640×512 pixels without binning. The moving average (50 frame window) was subtracted from the acquired sequence of images to remove the background signals. Subsequently, localization and tracking of the injected droplets was performed using a simple and extendable open-source framework TrackNTrace [56]. The DOLI image was built with the accumulated localized positions after tracking while velocity and direction maps were computed from the calculated tracks.

Localization optoacoustic tomography

LOT was performed using a tomographic system comprising a spherical array of 512 ultrasound sensing elements (40 mm radius, 150° angular aperture; Imasonic SaS, Voray, France) [36]. OA signals were generated using a short-pulsed (~ 5 ns) Q-switched Nd:YAG laser (1064 nm; Innolas GmbH, Krailling, Germany), matched to the absorption peak of the microparticles. The trapezoidal array elements (~ 3.3×3.8 mm^2) have a central frequency of 7 MHz and > 80% bandwidth. The array features a central cylindrical aperture (8 mm diameter) and three lateral apertures (4 mm diameter, 45° elevation, 120° azimuthal spacing). Illumination was delivered through these apertures using a custom four-arm fiber bundle (CeramOptec GmbH, Bonn, Germany), providing approximately uniform surface illumination with optical fluence ~ 40 mJ/cm^2. OA signals were amplified (~ 40 dB), digitized at 40 MS/s using a custom data acquisition system (Falkenstein Mikrosysteme GmbH, Taufkirchen, Germany), and synchronized with the laser Q-switch. Raw signals were first bandpass-filtered (Butterworth, 0.2–8 MHz). A spatio-temporal singular value decomposition (SVD) filter was then applied to subsets of 1200 frames. Local intensity maxima, attributed to microparticle signals, were identified in each 3D frame. Candidate regions were cross-correlated with an experimentally measured point spread function (PSF), retaining detections with correlation coefficients > 0.4. Localizations were linked into trajectories using the Munkres algorithm (simpletracker.m, MathWorks; implementation by Yi Cao, 2009), with a maximum linking distance of 0.5 mm and a minimum track length of 60 points. This enabled detection of flow velocities up to ~ 50 mm/s, limited by the imaging frame rate. Velocities and direction maps were computed from frame-to-frame displacements.

Synthesis of fluorescent microdroplets

Microdroplets for DOLI were synthesized using a standard emulsification protocol [31]. Briefly, dichloromethane (DCM) containing core/shell PbS/CdS quantum dots (QDs; NBDY-0038, 1600 nm

emission, Nirmidas Biotech, USA) was used as the dispersed phase. 50 µL of this QDs dispersion was added to 1 mL of deionized water containing 3% (v/v) Tween 20 (P1379, Sigma-Aldrich, Germany). The mixture was vortexed for 30 s and passed through a 40 µm cell strainer to obtain a relatively uniform microdroplet suspension. The synthesized droplets were quantified at 2×10^7 particles/mL using a hemocytometer and optical microscopy (Primostar 3, ZEISS, Germany).

Synthesis of microparticles for LOT

Microparticles for LOT were prepared as previously described [35]. Citrate-stabilized CuS nanoparticles were synthesized using a modified protocol. Briefly, $CuCl_2$ (50 mM, 1 mL) and sodium citrate (34 mM, 1 mL) were added to 48 mL of deionized (DI) water under stirring at room temperature. After 5 min, Na_2S (1 M, 100 µL) was introduced, yielding a dark brown solution. The mixture was then heated to 90°C for 15 min until a dark-green color developed, followed by rapid cooling in an ice bath. Unreacted reagents were removed by centrifugation (15 mL filter units, 3350 RCF, 15 min; Multifuge 1S-R, Thermo Scientific), and the suspension was adjusted to 5 mL (9.087 mM). $CaCO_3$ microparticles (MPs) were synthesized by adding Na_2CO_3 (0.33 M, 0.5 mL) and $CaCl_2$ (0.33 M, 0.5 mL) to a BSA solution (40 mg/mL, 1 mL) under stirring at 30°C. After 30 s, stirring was stopped and particles were allowed to mature for 10 min. MPs were washed three times (60 g, 30 s; 5415 D, Eppendorf) and resuspended in 1 mL DI water. For loading, 1 mL of $CaCO_3$ MPs was mixed with 0.5 mL CuS NPs and subjected to repeated freeze–thaw cycles (−20°C, 30 min, followed by thawing at room temperature). After every two cycles, particles were collected by centrifugation and redispersed to allow the addition of 0.5 mL of fresh CuS NPs. This process was repeated for a total of 14 cycles to achieve high loading efficiency. The resulting CuS-loaded $CaCO_3$ MPs were coated with polydopamine (PDA) by incubation in dopamine solution (4.35 mM, 1.5 mL, Tris buffer) under stirring for 3 h at room temperature. The final $CaCO_3$@CuS/PDA MPs were washed, resuspended in 1 mL PBS, and quantified at 2.5×10^8 particles/mL using a hemocytometer and optical microscopy (Primostar 3, ZEISS, Germany).

Animal experiments

All animal experiments were conducted in accordance with the Swiss Federal Act on Animal Protection and approved by the Cantonal Veterinary Office Zurich (ZH079/2022). All animals used in this study were housed in ventilated cages inside a temperature-controlled room under a 12-h dark/light cycle. The temperature was 21 ± 1°C, with a relative humidity of 55 ± 10%. Pelleted food and water were provided ad libitum. Triple-transgenic mice carrying mutations associated with familial AD (B6;129-Psen1^{tm1Mpm}Tg(APPSwe,tauP301L)1Lfa/Mmjax; The Jackson Laboratory) and WT controls on the same genetic background (B6129SF2/J; The Jackson Laboratory) were used in this study. Specifically, n = 5 AD and n = 4 WT mice were used for DOLI experiments, while n = 5 AD and n = 5 WT mice were used for LOT experiments. All mice were between 80 and 100 weeks of age.

Data analysis and statistics

Data processing and analysis were performed using MATLAB R2022a (MathWorks, USA). Analyses were conducted within selected regions of interest (ROIs) with size 1.2×1.2 mm^2 for DOLI and 1.2×1.2×1.2 mm^3 for LOT. Specifically, the mean velocity, vascular density (vascularity), and mean vessel tortuosity was calculated in the selected regions. The mean velocity was calculated from the velocity maps. The vascularity was calculated as the number of pixels (voxels) for which a track exists and a velocity value was assigned. The vascularity values were normalized to the average value for WT mice across all ROIs. Mean vessel tortuosity in the selected DOLI regions was calculated from the direction map. Specifically, the gradient of the direction map was calculated to estimate relative angular changes between pixels, where pixels with no velocity assigned were set to NaN. The tortuosity values were calculated as the sum of the valid (not NaN) pixels of the modulus of the gradient in the ROIs. For LOT, direction maps were calculated as the angles with respect to the *xy*, *xz*, and *yz* planes. Gradients were calculated for all three maps, and the tortuosity values were calculated as the sum of the moduli of all three gradients in the ROIs. Bar graphs display mean values ± standard deviation (SD). Statistical significance was assessed using an unpaired two-tailed Student's *t*-test, with $p < 0.05$ considered statistically significant.

Declarations

Code availability

The custom code developed and used in this study is available from the corresponding author upon reasonable request for academic research purposes.

Competing interests

The authors declare no competing interests.

Author Contribution

X.L.D-B. conceived the study and designed the experiments. X.L.D-B., L.T., and Q.Y. performed the experiments. X.L.D-B., L.T., Q.Y., D.S., and L.N. processed and analyzed the data. X.L.D-B. and D.R. supervised the project. X.L.D-B., L.T., and Q.Y. wrote the manuscript. All authors contributed to manuscript revision and approved the final version.

Acknowledgement

X.L.D-B and D.R. acknowledge support from ETH (ETH grant 25-1 ETH-033). We thank Diana Kindler for excellent technical assistance.

Data Availability

The primary data supporting the findings of this study are included in the main manuscript and Supplementary Information. Raw datasets are available from the corresponding author upon reasonable request for academic research purposes.

References

1. Makedonov, I., Black, S. & MacIntosh, B. Cerebral small vessel disease in aging and A lzheimer's disease: a comparative study using MRI and SPECT. *European journal of neurology* **20**, 243-250 (2013).
2. Van Der Flier, W. M. *et al.* Vascular cognitive impairment. *Nature reviews Disease primers* **4**, 18003 (2018).
3. Bailey, T. L., Rivara, C. B., Rocher, A. B. & Hof, P. R. The nature and effects of cortical microvascular pathology in aging and Alzheimer's disease. *Neurological research* **26**, 573-578 (2004).
4. Anderle, S., Dixon, M., Quintela-Lopez, T., Sideris-Lampretsas, G. & Attwell, D. The vascular contribution to cognitive decline in ageing and dementia. *Nature Reviews Neuroscience* **26**, 591-606 (2025).
5. Love, S. & Miners, J. S. Cerebrovascular disease in ageing and Alzheimer's disease. *Acta neuropathologica* **131**, 645-658 (2016).
6. Kisler, K., Nelson, A. R., Montagne, A. & Zlokovic, B. V. Cerebral blood flow regulation and neurovascular dysfunction in Alzheimer disease. *Nature Reviews Neuroscience* **18**, 419-434 (2017).
7. Beaudin, A. E. *et al.* Cerebrovascular reactivity across the entire brain in cerebral amyloid angiopathy. *Neurology* **98**, e1716-e1728 (2022).
8. Zhang, H. *et al.* Cerebral blood flow in mild cognitive impairment and Alzheimer's disease: A systematic review and meta-analysis. *Ageing research reviews* **71**, 101450 (2021).
9. Rensma, S. P. *et al.* Microvascular dysfunction is associated with worse cognitive performance: the Maastricht study. *Hypertension* **75**, 237-245 (2020).
10. Steinman, J., Sun, H.-S. & Feng, Z.-P. Microvascular alterations in Alzheimer's disease. *Frontiers in cellular neuroscience* **14**, 618986 (2021).
11. Cai, C. *et al.*
12. Zimmerman, B., Rypma, B., Gratton, G. & Fabiani, M. Age-related changes in cerebrovascular health and their effects on neural function and cognition: A comprehensive review. *Psychophysiology* **58**, e13796 (2021).
13. Deshpande, A. *et al.* Cerebrovascular morphology: Insights into normal variations, aging effects and disease implications. *Journal of Cerebral Blood Flow & Metabolism* **45**, 1249-1264 (2025).
14. Hosoki, S. *et al.* Molecular biomarkers for vascular cognitive impairment and dementia. *Nature Reviews Neurology* **19**, 737-753 (2023).
15. Fisher, R. A., Miners, J. S. & Love, S. Pathological changes within the cerebral vasculature in Alzheimer's disease: New perspectives. *Brain Pathology* **32**, e13061 (2022).

16. Hong, H. *et al.* The relationship between amyloid pathology, cerebral small vessel disease, glymphatic dysfunction, and cognition: a study based on Alzheimer's disease continuum participants. *Alzheimer's research & therapy* **16**, 43 (2024).
17. Tarawneh, R. Microvascular contributions to Alzheimer disease pathogenesis: is Alzheimer disease primarily an endotheliopathy? *Biomolecules* **13**, 830 (2023).
18. Jullienne, A. *et al.* Progressive vascular abnormalities in the aging 3xTg-AD mouse model of Alzheimer's disease. *Biomedicines* **10**, 1967 (2022).
19. Li, Y. *et al.* Aging-associated changes in cerebral vasculature and blood flow as determined by quantitative optical coherence tomography angiography. *Neurobiology of aging* **70**, 148-159 (2018).
20. Yan, F. *et al.* Dimension-based quantification of aging-associated cerebral microvasculature determined by optical coherence tomography and two-photon microscopy. *Journal of biophotonics* **17**, e202300409 (2024).
21. Meng, G. *et al.* Ultrafast two-photon fluorescence imaging of cerebral blood circulation in the mouse brain in vivo. *Proceedings of the National Academy of Sciences* **119**, e2117346119 (2022).
22. Couture, O., Hingot, V., Heiles, B., Muleki-Seya, P. & Tanter, M. Ultrasound localization microscopy and super-resolution: A state of the art. *IEEE transactions on ultrasonics, ferroelectrics, and frequency control* **65**, 1304-1320 (2018).
23. Yi, H.-m., Lowerison, M. R., Song, P.-f. & Zhang, W. A review of clinical applications for super-resolution ultrasound localization microscopy. *Current medical science* **42**, 1-16 (2022).
24. Thalgott, J. H. *et al.* Non-invasive characterization of pericyte dysfunction in mouse brain using functional ultrasound localization microscopy. *Nature Biomedical Engineering* **10**, 214-230 (2026).
25. Liao, Y., Chen, X., Chen, S., Lin, H. & Shen, Y. in *2022 IEEE International Ultrasonics Symposium (IUS)*. 1-4 (IEEE).
26. Lowerison, M. R. *et al.* Aging-related cerebral microvascular changes visualized using ultrasound localization microscopy in the living mouse. *Scientific reports* **12**, 619 (2022).
27. Huang, H. *et al.* High-spatiotemporal-resolution ultrasound flow imaging to determine cerebrovascular hemodynamics in Alzheimer's disease mice model. *Advanced Science* **10**, 2302345 (2023).
28. Lin, H. *et al.* Super-resolution ultrasound imaging reveals temporal cerebrovascular changes with disease progression in female 5× FAD mouse model of Alzheimer's disease: correlation with pathological impairments. *EBioMedicine* **108** (2024).
29. Lowerison, M. R. *et al.* Super-resolution ultrasound reveals cerebrovascular impairment in a mouse model of Alzheimer's disease. *The Journal of Neuroscience* **44**, e1251232024 (2024).
30. Negri, S. *et al.* A Minimally Invasive Framework Reveals Region-Specific Cerebrovascular Remodeling in Aging Using Intravital Functional Ultrasound Imaging and Ultrasound Localization Microscopy (fUS-ULM). *Advanced Science* **13**, e10754 (2026).

31. Zhou, Q., Chen, Z., Robin, J., Deán-Ben, X.-L. & Razansky, D. Diffuse optical localization imaging for noninvasive deep brain microangiography in the NIR-II window. *Optica* **8**, 796-803 (2021).
32. Zhou, Q. *et al.* Depth-resolved localization microangiography in the NIR-II Window. *Advanced Science* **10**, 2204782 (2023).
33. Deán-Ben, X. L. *et al.* Deep optoacoustic localization microangiography of ischemic stroke in mice. *Nature Communications* **14**, 3584 (2023).
34. Nozdriukhin, D., Lyu, S., Razansky, D. & Deán-Ben, X. L. Large-scale super-resolution optoacoustic imaging facilitated by FeNP/ICG-loaded coreless polyelectrolyte microcapsules. *Theranostics* **15**, 6412 (2025).
35. Tang, L. *et al.* Scalable copper sulfide formulations for super-resolution optoacoustic brain imaging in the second near-infrared window. *Small Methods* **9**, 2400927 (2025).
36. Ni, R. *et al.* Multiscale optical and optoacoustic imaging of amyloid-β deposits in mice. *Nature Biomedical Engineering* **6**, 1031-1044 (2022).
37. Nozdriukhin, D. *et al.* Three-dimensional microangiography of the mouse brain using super-resolution ultrasound and optoacoustic imaging with a spherical array transducer. *Photoacoustics*, 100823 (2026).
38. Blennow, K., de Leon, M. J. & Zetterberg, H. Alzheimer's disease. *The lancet* **368**, 387-403 (2006).
39. Gazestani, V. *et al.* Early Alzheimer's disease pathology in human cortex involves transient cell states. *Cell* **186**, 4438-4453. e4423 (2023).
40. Van De Haar, H. J. *et al.* Blood-brain barrier leakage in patients with early Alzheimer disease. *Radiology* **281**, 527-535 (2016).
41. Jagust, W. Imaging the evolution and pathophysiology of Alzheimer disease. *Nature Reviews Neuroscience* **19**, 687-700 (2018).
42. Madsen, L. S. *et al.* Capillary dysfunction correlates with cortical amyloid load in early Alzheimer's disease. *Neurobiology of Aging* **123**, 1-9 (2023).
43. Salat, D. H. *et al.* Age-associated alterations in cortical gray and white matter signal intensity and gray to white matter contrast. *Neuroimage* **48**, 21-28 (2009).
44. Gorshkova, O. Changes in rat cerebral blood flow velocities at different stages of aging. *Journal of Evolutionary Biochemistry and Physiology* **59**, 569-576 (2023).
45. Elzinga, S. E. *et al.* Metabolic stress and age drive inflammation and cognitive decline in mice and humans. *Alzheimer's & Dementia* **21**, e70060 (2025).
46. Bennett, H. C. *et al.* Aging drives cerebrovascular network remodeling and functional changes in the mouse brain. *Nature communications* **15**, 6398 (2024).
47. Berthiaume, A.-A. *et al.* Pericyte remodeling is deficient in the aged brain and contributes to impaired capillary flow and structure. *Nature Communications* **13**, 5912 (2022).
48. Stamenkovic, S. *et al.* Impaired drainage through capillary-venous networks contributes to age-related white matter loss. *BioRxiv* (2024).

49. Tang, L. *et al.* Super-resolution optoacoustic imaging of cerebral microcirculation with indocyanine green microcapsules. *ACS photonics* **11**, 4642-4647 (2024).
50. Nozdriukhin, D. *et al.* Multifunctional microflowers for precise optoacoustic localization and intravascular magnetic actuation in vivo. *Advanced Healthcare Materials* **14**, 2404242 (2025).
51. Nozdriukhin, D. *et al.* Multiparametric super-resolution optoacoustic imaging with ICG-tagged microbubbles. *Materials Today Bio* **32**, 101865 (2025).
52. Nozdriukhin, D. *et al.* Nanoporous submicron gold particles enable nanoparticle-based localization optoacoustic tomography (nanoLOT). *Small* **20**, 2404904 (2024).
53. Alfotawi, R. *et al.* Assessment of novel surgical procedures using decellularised muscle and bioactive ceramic: a histological analysis. *Journal of Materials Science: Materials in Medicine* **32**, 113 (2021).
54. Wang, Z. *et al.* Acoustic Transparency Enabling Functional Ultrasound Imaging Through Mouse and Human Skulls. *bioRxiv*, 2025.2008. 2022.671878 (2025).
55. Nißler, R. *et al.* Unlocking NIR-II Photoluminescence in 2D Copper Tetrasilicate Nanosheets through Flame Spray Synthesis. *Advanced Materials* **37**, 2503159 (2025).
56. Stein, S. C. & Thiart, J. TrackNTrace: A simple and extendable open-source framework for developing single-molecule localization and tracking algorithms. *Scientific reports***6**, 37947 (2016).

Figures

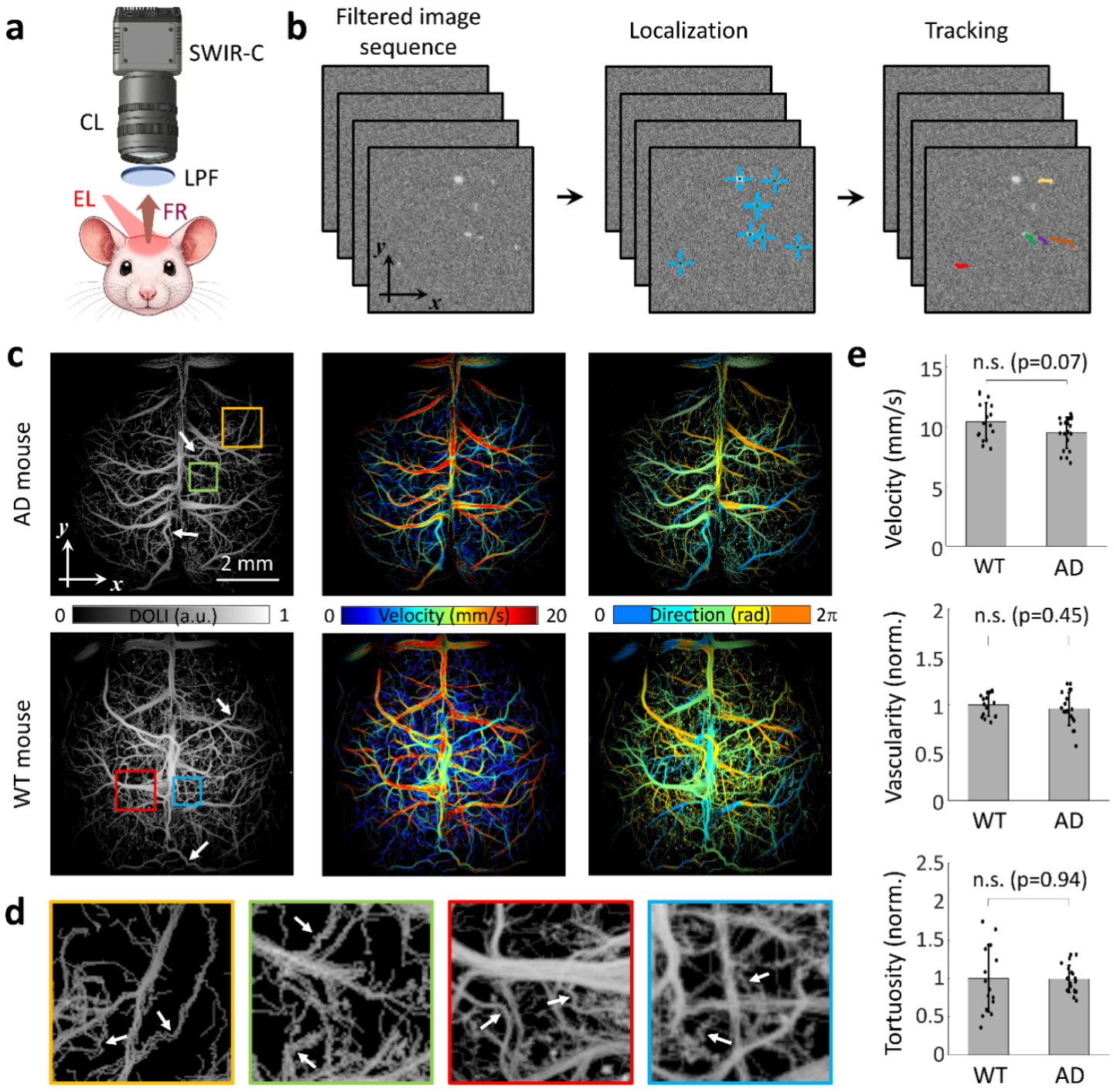


Figure 1

Transcranial optical microangiography of the entire murine cortex. (a) Lay-out of the diffuse optical localization imaging (DOLI) set-up. SWIR-C – short-wave infrared camera, CL – camera lens, LPF – long pass filter, EL – excitation light, FR – fluorescence response. (b) Image processing pipeline including filtering for background signal removal, localization of the intravenously injected microdroplets, and tracking of these droplets as they flow in the bloodstream. (c) Representative DOLI images of an Alzheimer's disease (AD) mouse (top) and a wild-type (WT) mouse (bottom) of approximately the same age. Velocity and angular direction maps for the same mice are also shown. (d) Zoomed-in views of

selected regions indicated in panel c. (e) Comparison of the velocity, vascularity (vascular density) and vessel tortuosity in approximately matched cortical regions in WT and AD mice. Arrows point to convoluted and tortuous vessels at different scales.

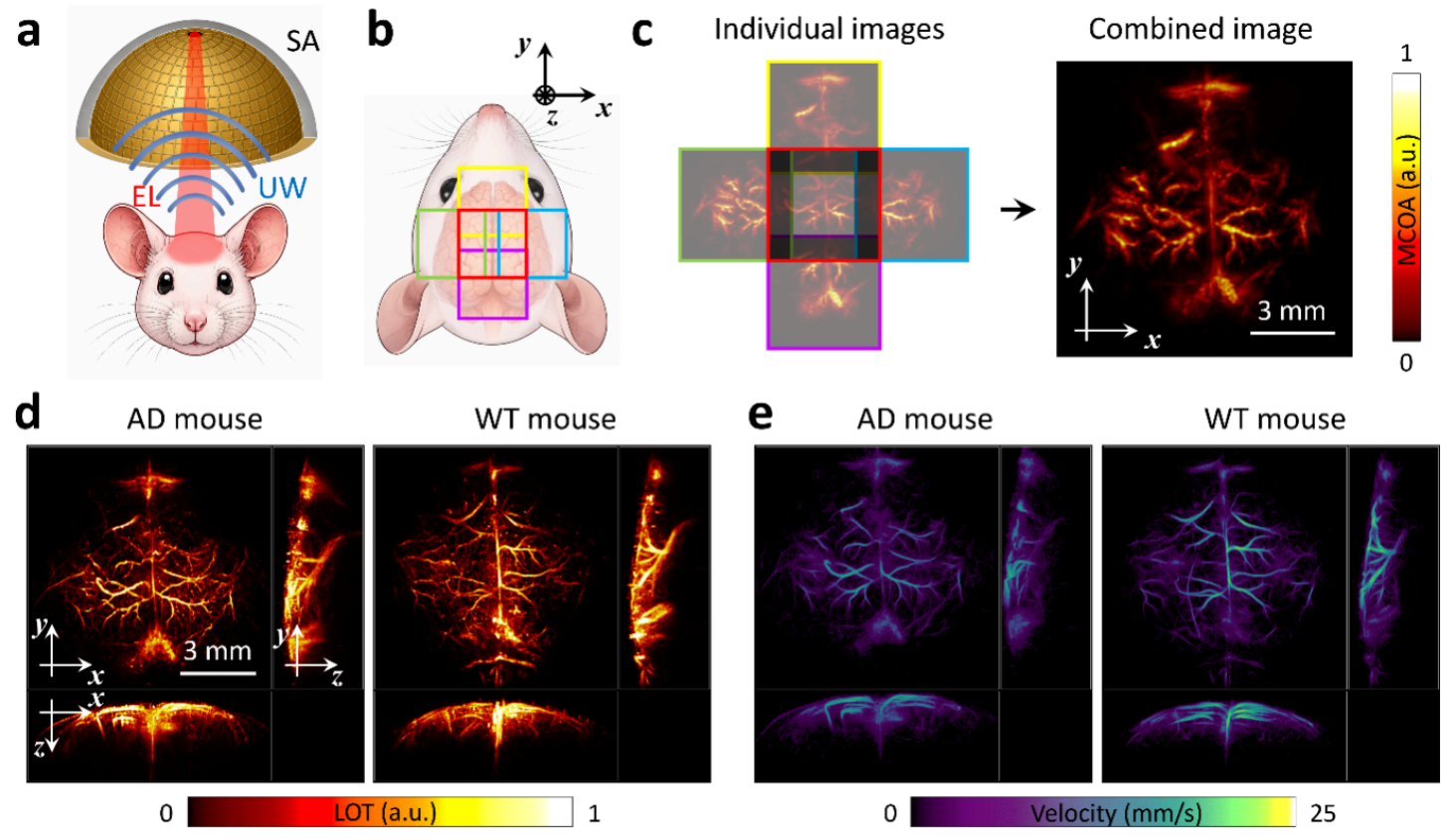


Figure 2

Non-invasive optoacoustic microangiography of the entire murine cortex. (a) Lay-out of the optoacoustic (OA) tomographic imaging system used to implement localization optoacoustic tomography (LOT). SA – spherical array, EL – excitation light, UW – ultrasound waves. (b) Regions covered with LOT for 5 positions of the array scanned across the murine cortex. (c) Reconstructed motion contrast optoacoustic (MCOA) images for the 5 positions of the array. The MCOA image of the entire cortex is built by combining individual images. Maximum intensity projections (MIPs) along the depth direction are shown. (d) LOT images of the entire murine cortex of an Alzheimer's disease (AD) mouse and an age-matched wild-type (WT) mouse. MIPs along all three Cartesian directions are shown. (e) Velocity maps for the same AD and WT mice. MIPs along all three Cartesian directions are shown.

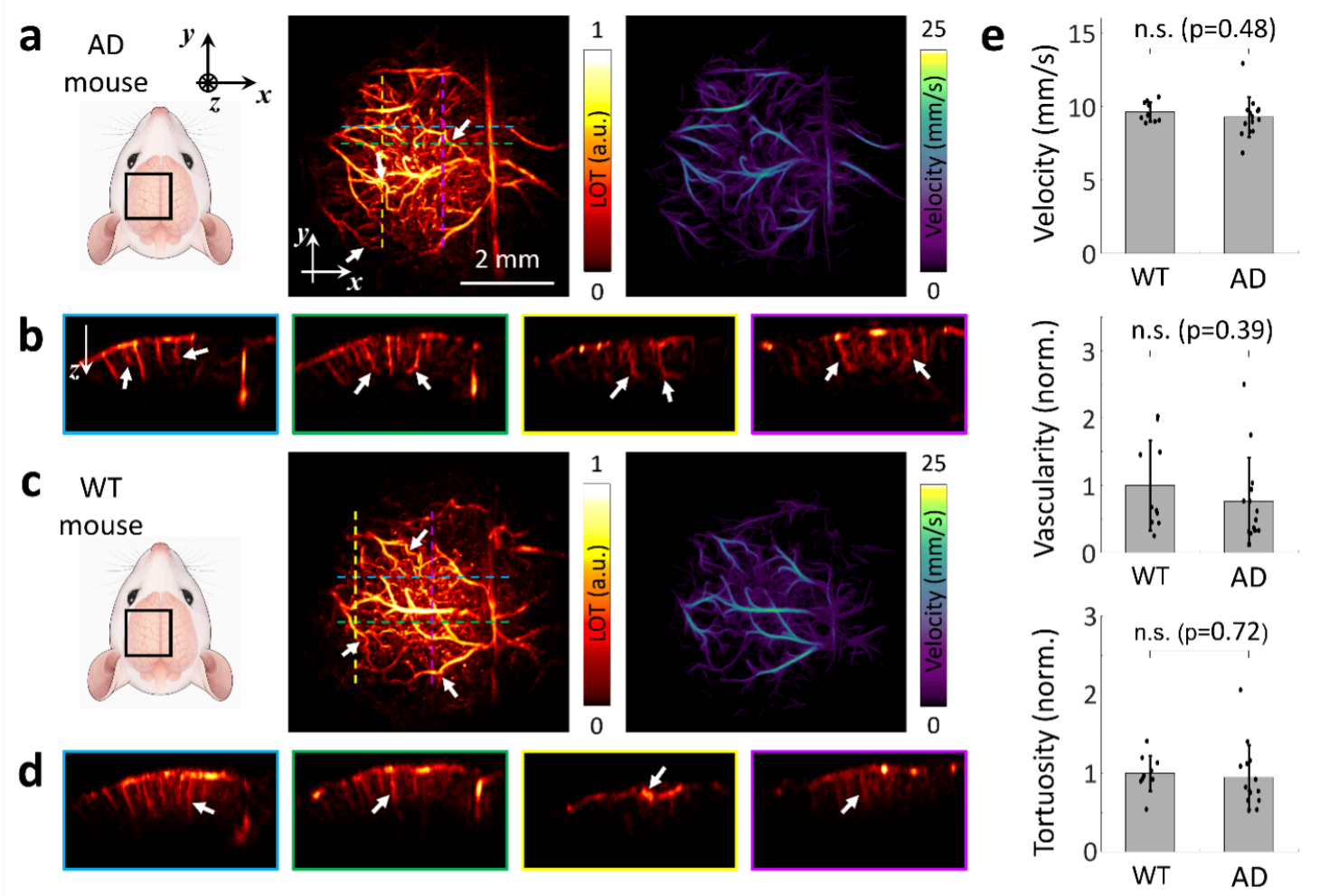


Figure 3

Assessment of microvascular alterations in superficial and penetrating cortical vessels. (a) Imaged region in an AD mouse (left), along with maximum intensity projections (MIPs) along the depth direction of the localization optoacoustic tomography (LOT) image (middle) and the corresponding velocity map (right). (b) Cross-sectional views of penetrating vessels for the sections indicated in panel a. (c) Imaged region in a WT mouse (left), along with MIPs along the depth direction of the LOT image (middle) and the corresponding velocity map (right). (d) Cross-sectional views of penetrating vessels for the sections indicated in panel c. (e) Comparison of the velocity, vascularity (vascular density) and vessel tortuosity in approximately matched cortical regions in WT and AD mice. Arrows point to convoluted and tortuous vessels at different scales.

Supplementary Files

This is a list of supplementary files associated with this preprint. Click to download.

- Tang2026npjagingsupplementary.docx